

HYBRID LES-RANS: INLET BOUNDARY CONDITIONS FOR FLOWS INCLUDING RECIRCULATION

Lars Davidson

Division of Fluid Dynamics, Department of Applied Mechanics
Chalmers University of Technology, SE-412 96 Göteborg, Sweden
<http://www.tfd.chalmers.se/~lada>, lada@chalmers.se

ABSTRACT

The paper evaluates a new method for prescribing synthesized turbulent inlet boundary conditions. When making LES, DES or hybrid LES-RANS, a precursor channel DNS is often used. The disadvantage of this method is that it is difficult to re-scale the DNS fluctuations to higher Reynolds numbers. In the present work, synthesized isotropic turbulent fluctuations are generated at the inlet plane with a prescribed turbulent length scale and energy spectrum. A large number of independent realizations are generated. A correlation in time between these realization is introduced via an asymmetric, non-truncated time filter. In this way the turbulent time scale of the synthesized isotropic turbulent fluctuations is prescribed.

The method has previously been validated for DNS at $Re_\tau = 500$ (Davidson 2007). In that study it was found that the present approach is at least as good as using inlet boundary conditions from a pre-cursor DNS. This method has also been employed using hybrid LES-RANS for channel flow at $Re_\tau = 2000$ (Davidson 2007).

In the present study it is employed in hybrid LES-RANS of the flow in an asymmetric diffuser, the flow around a three-dimensional hill and the flow over the downstream part of a bump.

INTRODUCTION

Isotropic synthesized fluctuations based on the method of Kraichnan (1970) have often been used to generate turbulent fluctuations. In this method an energy spectrum is prescribed that yields the amplitude of the fluctuations as a function of wave number. Non-isotropic fluctuations have been investigated (Le and Moin 1994; Batten et al. 2004; Smirnov et al. 2001; Billson et al. 2004; Billson 2004) where the fluctuations were scaled so that the time-averaged synthesized fluctuations match a prescribed Reynolds stress tensor. A disadvantage of this kind of scaling is that the prescribed spectrum, and hence the two-point correlation, are modified if – as is always the case in real flows – the Reynolds stress tensor is non-homogeneous.

To achieve correlation in time, Fourier series were applied in time in the same way as in space in most of the works cited above. In Lee et al. (1992) a method was also investigated where a three-dimensional box with generated fluctuations was convected across the inlet plane; in this way fluctuation correlations in the streamwise directions were transformed into correlations in time. In the work of Billson et al. (2004) correlation in time is defined by an asymmetric infinite time filter. The method offers a convenient way to prescribe turbulent length and time scales independently. This method is adopted in the present work.

A method based partly on synthesized fluctuations was recently presented and is called the vortex method (Jarrin et al. 2006). It is based on a superposition of coherent eddies where each eddy is described by a shape function that is localized in space. The eddies are generated randomly in the inflow plane and then convected through

it. The method is able to reproduce first and second-order statistics as well as two-point correlations.

SYNTHESIZED TURBULENCE

A turbulent velocity field can be simulated using random Fourier modes. The velocity field is given by N random Fourier modes as

$$u'_i(x_j) = 2 \sum_{n=1}^N \hat{u}^n \cos(\kappa_j^n x_j + \psi^n) \sigma_i^n \quad (1)$$

where \hat{u}^n , ψ^n and σ_i^n are the amplitude, phase and direction of Fourier mode n . The highest wave number is defined based on mesh resolution $\kappa_{max} = 2\pi/(2\Delta)$. The smallest wave number is defined from $\kappa_1 = \kappa_e/p$, where κ_e corresponds to the energy-carrying eddies. Factor p should be larger than one to make the largest scales larger than those corresponding to κ_e . In the present work $p = 2$. The wavenumber space, $\kappa_{max} - \kappa_1$, is divided into N modes (typically 150 – 600), equally large, of size $\Delta\kappa$. A modified von Kármán spectrum is chosen. The amplitude of the fluctuations is set so that RMS is equal to the friction velocity at the inlet, i.e. $u_{rms} = v_{rms} = w_{rms} = u_{\tau, in}$.

A fluctuating velocity field is generated each time step as described above. They are independent of each other, however, and their time correlation will thus be zero. This is unphysical. To create correlation in time, new fluctuating velocity fields, \mathcal{U}'_i , are computed based on an asymmetric time filter.

$$(\mathcal{U}'_i)^m = a(\mathcal{U}'_i)^{m-1} + b(u'_i)^m \quad (2)$$

where m denotes the time step number and $a = \exp(-\Delta t/T)$. This asymmetric time filter resembles the spatial digital filter presented by Klein et al. (2003). The second coefficient is taken as $b = (1 - a^2)^{0.5}$ which ensures that $\langle \mathcal{U}'_i{}^2 \rangle = \langle u'^2 \rangle$ ($\langle \cdot \rangle$ denotes averaging). The time correlation of \mathcal{U}'_i will be equal to $\exp(-\Delta t/T)$, and thus Eq. 2 is a convenient way to prescribe the turbulent time scale of the fluctuations. The inlet boundary conditions are prescribed as

$$\bar{u}_i(0, y, z, t) = U_{i, in}(y) + \mathcal{U}'_{i, in}(y, z, t) \quad (3)$$

where $\mathcal{U}'_{i, in} = (\mathcal{U}'_i)^m$. The mean inlet profiles, $U_{i, in}(y)$, are either set from experiments or, for example, from the law of the wall.

The turbulent length scale and time scale are $L_t = 0.1$ and $T_t = 0.05$, respectively, scaled with the boundary layer thickness and the friction velocity at the inlet.

The synthetic fluctuations created with the method presented above yield homogeneous turbulence in the inlet plane, i.e. u_{rms} , v_{rms} , and w_{rms} are constant (and equal) across the entire inlet plane. The fluctuations could of course be scaled so that their RMS follow some prescribed y variation, but as pointed out in Davidson (2007), this would destroy the two-point correlations that have implicitly been prescribed via the von Kármán spectrum. However, the fluctuations need to be reduced near the wall so that they

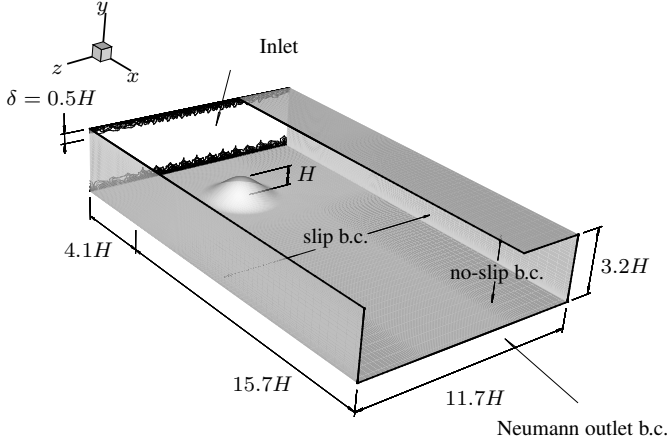


Figure 1: 3D hill. Computational domain. Hill crest at $x = z = 0$. Extension of hill: $-2 \leq x/H \leq 2$; $-2 \leq z/H \leq 2$.

go smoothly to zero as the wall is approached (this is done for $y/\delta_{in} \lesssim 0.004$).

At the outer edge of the boundary layer, the synthetic fluctuations must also be modified in some way (an exception is the diffuser flow, for which the boundary layer is fully developed). To achieve this, the fluctuations are multiplied by a blending function

$$f_{bl} = \min \{0.5 [1 - \tanh(n - \delta_{in})/b], 0.1\} \quad (4)$$

where n is the distance to the closest wall and b is the distance over which f_{bl} goes from 1 to 0. Freestream turbulence is prescribed by not letting f_{bl} become smaller than 0.1.

THE NUMERICAL METHOD

An incompressible, finite volume code is used (Davidson and Peng 2003). For space discretization, central differencing is used for all terms. The Crank-Nicolson scheme (with $\alpha = 0.6$) is used for time discretization of all equations. The numerical procedure is based on an implicit, fractional step technique with a multigrid pressure Poisson solver (Emvin 1997) and a non-staggered grid arrangement.

THE HYBRID LES-RANS MODEL

Hybrid LES-RANS is used. A one-equation for the modelled turbulent kinetic energy, k_T , is solved in the entire domain. URANS is employed near the wall and LES is used in the remaining part of the domain. The only difference between the two regions is the definition of the length scale when computing the turbulent viscosity and the dissipation term in the k_T equation. The length scale in the URANS is proportional to the wall distance whereas in the LES region it is taken as the cell volume up to the power of $1/3$. For more detail, see Davidson and Billson (2006); no forcing is used at the interface.

RESULTS

3D hill flow

A $162 \times 82 \times 130$ (x, y, z) mesh is used (1.7 million cells). The Reynolds number is 130 000 based on the hill height. The inlet and the crest of the axis-symmetric hill are located at $x = -4.1H$ and $x = 0$, respectively. The inlet boundary layer thickness is $\delta_{in}/H = 0.5$. The grid resolution at the inlet expressed in wall units is $\Delta x^+ = 280$ and $\Delta z^+ = 120$, which correspond to $\Delta x/\delta_{in} = 0.12$ and $\Delta z/\delta_{in} = 0.051$, respectively. The first near-wall cell center is located at $y^+ = 1.5$. The matching line is defined along an instantaneous streamline; for more detail, see Davidson and Dahlström (2005b)

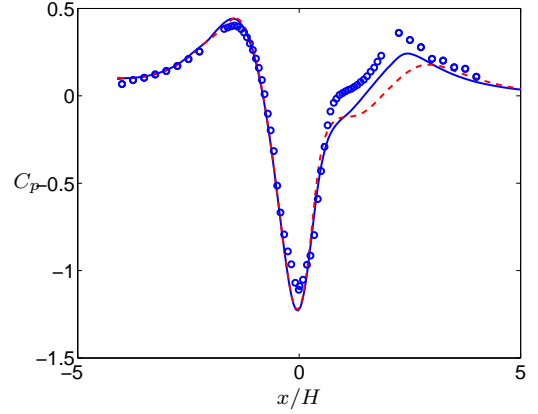


Figure 2: 3D hill. Pressure coefficient. $z = 0$. — : inlet fluctuations; - - - : no inlet fluctuations; markers: experiments (Byun et al. 2004).

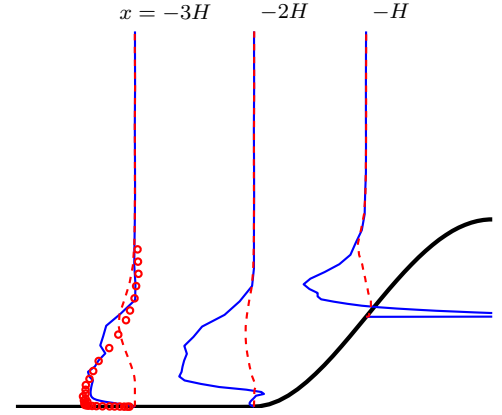


Figure 3: 3D hill. Resolved shear stresses. $z = 0$. — : inlet fluctuations; - - - : no inlet fluctuations; markers: experiments (Byun et al. 2004).

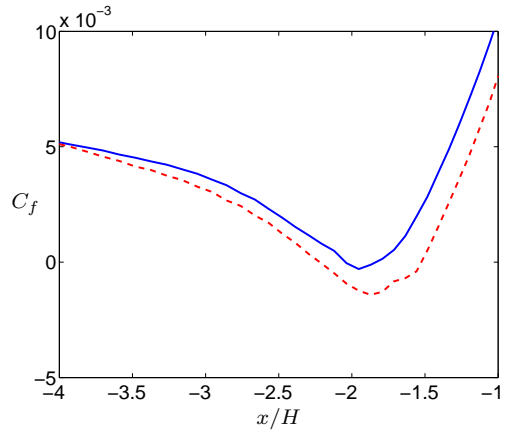


Figure 4: 3D hill. Friction coefficient. $z = 0$. — : inlet fluctuations; - - - : no inlet fluctuations.

Figure 2 presents the surface pressure over the hill obtained with and without inlet fluctuations. As can be seen, better agreement is obtained in the former case. The resolved shear stresses at the wind-side of the hill are shown in Fig. 3, and as can be seen only small resolved stresses are generated when steady inlet boundary conditions are employed. When fluctuating inlet conditions are used, the resolved shear stress profile at $x = -3H$ agrees well with experiments. Because only small resolved stresses are created when steady inlet boundary conditions are used, the skin friction is consequently smaller than when inlet fluctuations are used, see Fig. 4. Also, a small

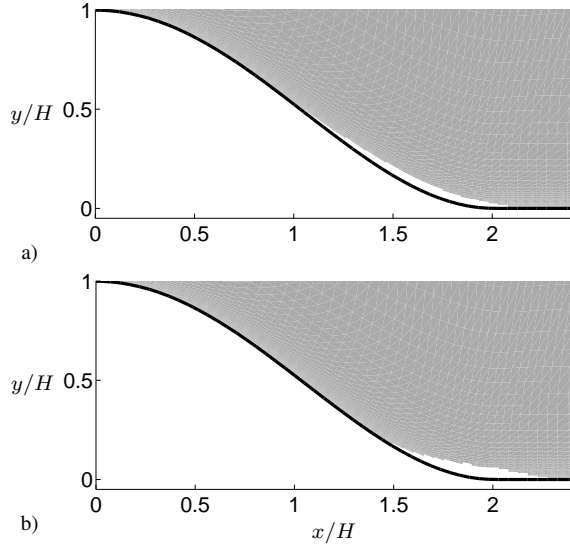


Figure 5: 3D hill. White region indicates backflow region. $z = 0$. a) Fluctuating inlet boundary conditions; b) steady inlet boundary conditions.

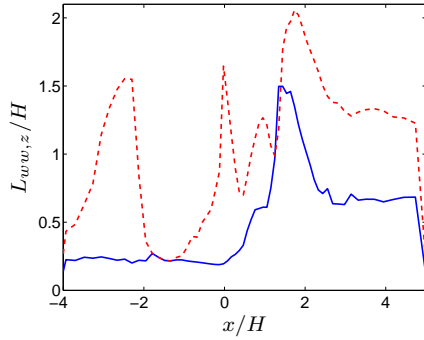


Figure 6: 3D hill. Integral length scale, $L_{ww,z}$, normalized by the hill height, H . L is evaluated at approximately $0.05H$ from the wall. —: inlet fluctuations; - - -: steady inlet.

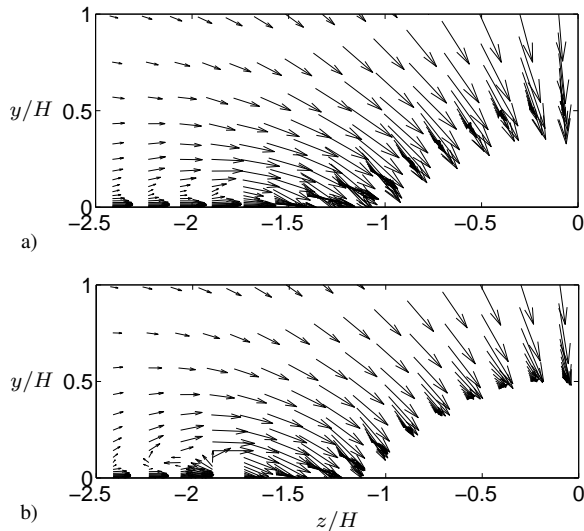


Figure 7: 3D hill. Velocity vectors at $x = H$. Every 2nd (3rd) vector plotted in the y (z) coordinate direction. a) Fluctuating inlet boundary conditions; b) steady inlet boundary conditions.

recirculation bubble is formed at the foot ($x/H \simeq -2$) of the hill for

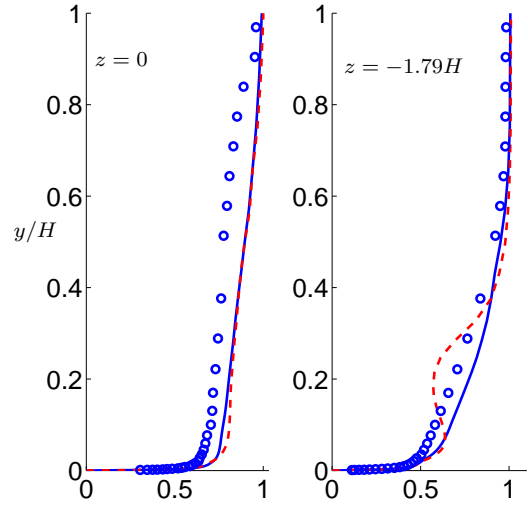


Figure 8: Streamwise velocity component $\langle \bar{u} \rangle / U_{in}$ at $x = 3.69H$. —: Fluctuating inlet boundary conditions; - - -: steady inlet boundary conditions; o: experiments (Byun et al. 2004)

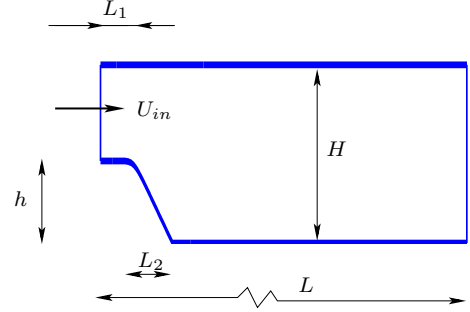


Figure 9: Onera bump. Computational domain (not to scale).

steady inlet conditions, which is not the case for fluctuating inlet conditions, see Fig. 4.

Because the computed flow accelerating over the hill crest is fairly different for the two cases, the recirculation regions on the lee-side of the hill are also different, see Fig. 5. The flow separates much later with steady inflow conditions than with fluctuating inlet boundary conditions. The recirculating region in the latter case is in good agreement with experiments (Byun et al. 2004).

The integral length scale is computed as

$$L_{ww,z} = \frac{1}{w_{rms}(0)} \int_0^{W/2} \frac{w'(0)w'(z)dz}{w_{rms}(z)} \quad (5)$$

For steady inlet conditions, we have very little resolved turbulence on the wind-side of the hill, and hence the two-point correlations decay very slowly for increasing separation distance, z . This yields large integral length scales, $L_{ww,z}$, see Fig. 6. For fluctuating boundary conditions, the integral length scale is approximately $0.25H$ – i.e. half the inlet boundary layer thickness – up to the separation point. As expected, the integral length scale is large for both cases in the recirculation region.

Traces of the recirculating bubble formed at the wind-side can also be seen at $x = H$ in Fig. 7b at $(y/H, z/H) = (0.05, -1.8)$. Even at $x = 3.69H$ it is seen in the form of a velocity deficit in the streamwise velocity profile at $y \simeq 0.25H$, see Fig. 8. No recirculating bubble is seen for fluctuating inlet conditions (Fig. 7a).

Onera bump

Measurements were carried out by ONERA in the DESider project (Pailhas et al. 2008). $Re_h = 0.556 \cdot 10^6$ based on the

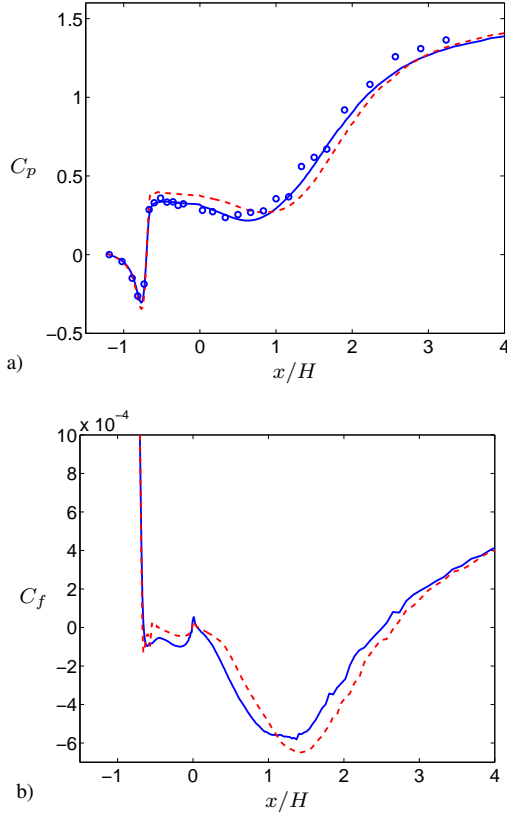


Figure 10: Onera bump. —: fluctuating inlet boundary conditions; - - -: steady inlet boundary conditions; ○: experiments (Pailhas et al. 2008). Lower wall. a) Pressure coefficient; b) friction coefficient.

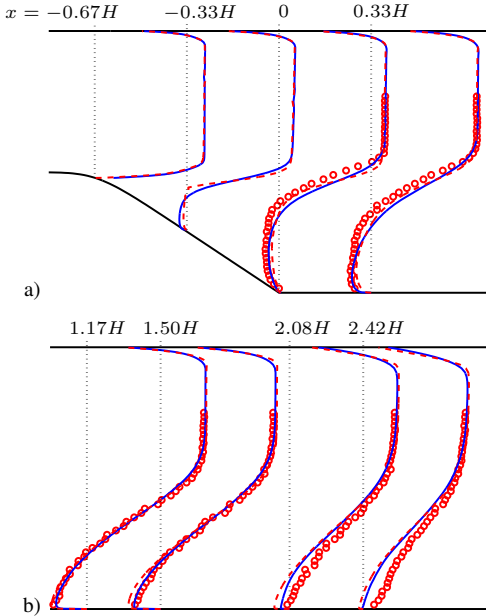


Figure 11: Onera bump. Streamwise mean velocity profiles. —: fluctuating inlet boundary conditions; - - -: steady inlet boundary conditions; ○: experiments (Pailhas et al. 2008).

bump height, h . The rectangular duct has the following dimensions (see Fig. 9): $W/H = 1.67$, $h/H = 0.46$, $L_1/H = 0.41$, $L_2/H = 0.81$, $H = 0.3m$. The inlet boundary layer thickness is $\delta_{in}/H = 0.043$. In the present study, simulations of the Onera bump

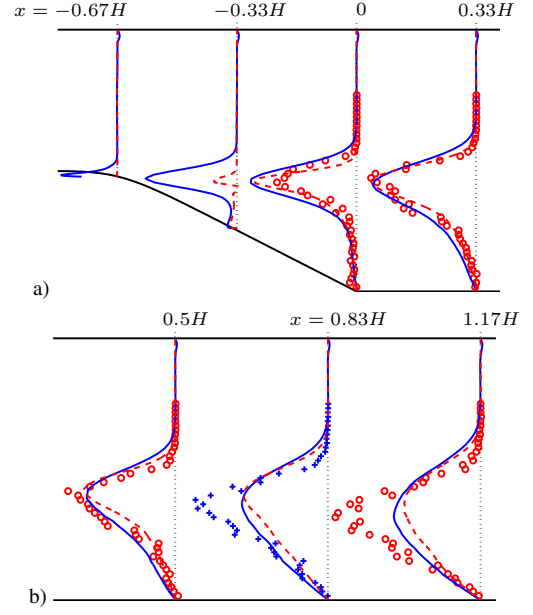


Figure 12: Onera bump. Resolved shear stresses. —: fluctuating inlet boundary conditions; - - -: steady inlet boundary conditions; markers: experiments (Pailhas et al. 2008).

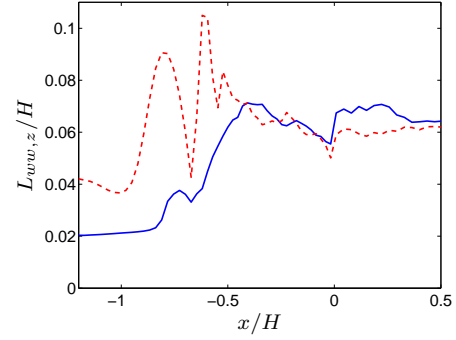


Figure 13: Onera bump flow. Integral length scale, $L_{ww,z}$, normalized by the channel height, H . $L_{ww,z}$ is evaluated at approximately $0.002\mathcal{H}(x) \simeq 0.6\delta_{in}$ where \mathcal{H} denotes the local channel height. —: inlet fluctuations; - - -: steady inlet.

have been carried out using only a slice in the central region and using period boundary conditions in the spanwise direction. The extent of the domain in the spanwise direction is $-0.61/2 \leq z/H \leq 0.61/2$ and in the streamwise direction it extends to $L/H = 8.86$. 32 cells are used in the z -direction ($\Delta z/H = 0.019$, $\Delta z/\delta_{in} = 0.44$). The grid in the $x - y$ plane has 224×120 cells. At the inlet $\Delta x/H = 0.0178$ ($\Delta x/\delta_{in} = 0.41$) and for $x/H \leq 1$ we have $\Delta x/H = 0.022$. In wall units this yields $\Delta z^+ = 1250$ and $\Delta z^+ = 1160$. The matching plane between LES and URANS is prescribed along fixed grid planes; the URANS region near the upper and the lower walls extends 12 wall-adjacent cells.

The Reynolds number for this flow is an order of magnitude larger than for the 3D hill, and the boundary layer is furthermore much thinner. Thus the grid is very coarse expressed in both inner and outer scaling. This makes it a very demanding test case.

Figure 10 shows the pressure coefficient and the skin friction along the lower wall. As can be seen, the agreement with the experimental pressure coefficient is good when using fluctuating inlet conditions, at least up to $x/H = 2$; for steady inlet conditions the agreement with experiments is less good. Further downstream the pressure coefficients indicate that the experimental flow recovers

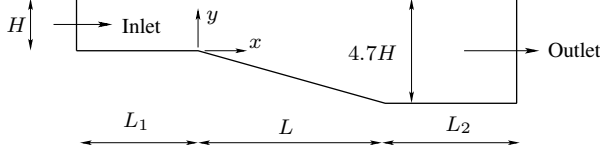


Figure 14: Plane asymmetric diffuser (not to scale). $L_1 = 7.9H$, $L = 21H$, $L_2 = 28H$. The spanwise width is $z_{max} = 4H$. The origin of $x - y - z$ is at the lower wall at the entrance of the diffuser.

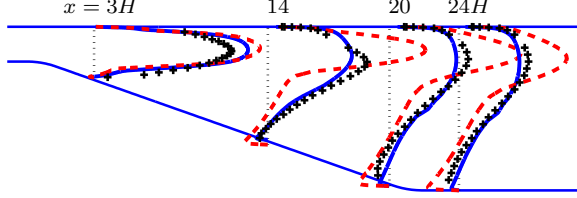


Figure 15: Diffuser flow. Mean velocities, $\langle \bar{u} \rangle$. — : fluctuating inlet boundary conditions; --- : steady inlet boundary conditions; + : experiments (Buice and Eaton 1997).

faster than the predicted flow. That the agreement between predictions with fluctuating inlet conditions and experiments is good for $x/H < 2$ and that the predicted recovery rate of the boundary layer is too slow compared with experiments can also be seen by looking at the velocity profiles in Fig. 11. Although the resolved shear stresses agree fairly well with experiments for $x/H \leq 0.5$, see Fig. 12, the peak value in the experimental stresses increases for $0.5 < x/H < 1.5$, whereas the peak value of the predicted stresses stays fairly constant. This explains why the predicted recovery rate is much faster than the predicted one. The question remains why the magnitude in the experimental shear stresses increases by some 20% between $x/H = 0.5$ and $x/H = 0.83$. At $x/H = 1.5$ the peak is 50% larger than at $x/H = 0.5$; it then starts to decay. The reason for the discrepancy in shear stresses may have to do with three-dimensional effects (recall that the side walls are not included in the simulations). Secondary streamwise vortices are created near the side walls and it may be that at $x/H = 0.5$ their influence reaches all the way to the centerplane; note, however, that the predicted velocity profiles agree well with experiments all the way up to $x/H = 1.17$. For larger x , the too small shear stresses start to affect the predicted velocity profiles.

In Fig. 12a it can be seen that, with steady inlet conditions, no resolved fluctuations are created for $x/H \leq -0.67$ and they are still much too small at $x/H = -0.33$. This explains the extremely thin shear layer that is seen in the velocity profile at $x/H = -0.33$ in Fig. 11a. the magnitude of the skin friction, $|C_f|$, is smaller than when fluctuating inlet boundary conditions are applied, see Fig. 10b. Furthermore, because the resolved shear stresses are smaller in the former case, a larger predicted recirculation bubble is obtained, see Fig. 10b.

The integration length scales are presented in Fig. 13. With fluctuating inlet conditions, $L_{ww,z}/H \simeq 0.02$ near the inlet which corresponds to $0.5\delta_{in}$. As was found for the 3D hill flow, when no inlet fluctuations are used the integration length scale becomes large near the inlet because of slowly decaying two-point correlations. In the separation region, $L_{ww,z}$ increases strongly for both cases.

Diffuser flow

The configuration is an asymmetric plane diffuser, with Reynolds number $Re = U_{b,in}H/\nu = 18\,000$, see Fig. 14. The opening angle is 10° . The location of the matching line is defined along an instantaneous streamline; for more detail, see Davidson and Dahlström (2005a). Figure 15 shows the velocity profiles in the diverging part of the diffuser. As can be seen, the results

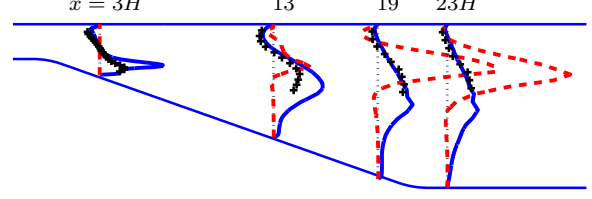


Figure 16: Diffuser flow. Resolved shear stresses, $\langle u'v' \rangle$. — : fluctuating inlet boundary conditions; --- : steady inlet boundary conditions; markers: experiments (Buice and Eaton 1997).

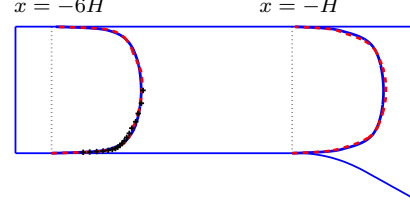


Figure 17: Diffuser flow. Inlet section of the domain. Mean velocities, $\langle \bar{u} \rangle$. — : fluctuating inlet boundary conditions; --- : steady inlet boundary conditions; markers: experiments (Buice and Eaton 1997).

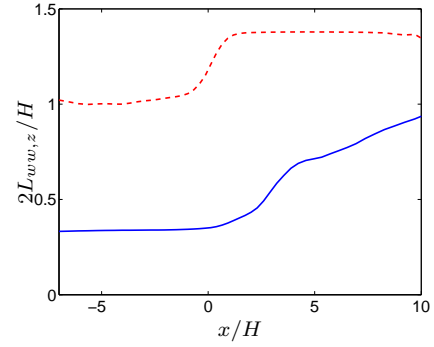


Figure 18: Diffuser flow. Integral length scale, $L_{ww,z}$, normalized by $H/2$. — : inlet fluctuations; --- : steady inlet.

with fluctuating inlet velocities are in much better agreement with experiments compared with when steady inlet conditions are used.

Figure 16 presents the resolved shear stresses. As can be seen, the resolved shear stresses for steady inlet boundary conditions are zero for $x/H \leq 3$. At the end of the diverging part, the resolved shear stresses for steady inlet conditions become very large in the upper part of the diffuser. The reason is that the velocity gradients in this regions are very large, see Fig. 15.

Although the turbulent shear stresses are very different for the two cases at the entrance of the diffuser, the mean profiles are very similar, see Fig. 17. In Davidson (2007) it was found that, at 10 channel heights downstream the inlet, very poor velocity profiles were predicted when white noise in time *or* space was used as inlet fluctuations. However, the grid in that study was much coarser ($(\Delta x^+, \Delta z^+) = (785, 393)$) than in the present study.

The integral length scales are presented in Fig. 18. When using fluctuating inlet conditions, the integral length scale normalized with the boundary layer thickness (i.e. $H/2$) is approximately 0.4 near the inlet. As for the 3D hill and the bump flows, steady inlet conditions yield a large length scale near the inlet (up to the throat). In the diverging region the integral length scale increases for both cases, as expected.

CONCLUSIONS

The present study evaluates a novel approach for generating fluctuating turbulent inlet boundary conditions. Synthetic isotropic fluctuating

tuations are superimposed on a mean velocity profile. The synthesized fluctuations are created by assuming a modified von Kármán spectrum. The RMS of the fluctuations and their integral length scale are supplied as input when creating the von Kármán spectrum. Previous work has shown that the amplitude can be taken as the friction velocity, u_τ , of the prescribed inlet mean velocity profile, and the integral length scale is taken to be 10% of the prescribed inlet boundary layer thickness. A number of realizations (in this work 5000) of velocity fluctuations are generated in the inlet plane and stored on disk. Each realization corresponds to the inlet fluctuations at one time step. The turbulent length scale of the fluctuations in the inlet plane corresponds to the prescribed integral length scale. However, the 5000 realizations are independent, i.e. the time correlation of the prescribed inlet turbulent fluctuations is zero. This is unphysical. In order to introduce correlation in time, an asymmetric time filter is used. This filter includes a turbulent time scale, which is taken as $0.1\delta_{in}/u_\tau$.

Three flows are simulated in the present work, namely, the 3D hill flow, the flow over a bump and the flow in a plane asymmetric diffuser. The results obtained using fluctuating inlet conditions are compared to those obtained using steady inlet boundary conditions. In all flows it is found that fluctuating inlet conditions are superior to steady inlet flow conditions. Resolved turbulent stresses are created in the inlet region in the former case, whereas no resolved stresses are created in the latter case. With fluctuating inlet conditions we obtained a predicted turbulent integral length scale in the inlet region that is approximately equal to half the boundary layer thickness for all three flows; this is physically realistic, although slightly too large. With steady inlet conditions, the predicted integral length scales are much too large because the two-point correlations decay much too slowly.

Acknowledgments.

This work was financed by the **DESider** project (Detached Eddy Simulation for Industrial Aerodynamics) which is a collaboration between Alenia, ANSYS-AEA, Chalmers University, CNRS-Lille, Dassault, DLR, EADS Military Aircraft, EUROCOPTER Germany, EDF, FOI-FFA, IMFT, Imperial College London, NLR, NTS, NU-MECA, ONERA, TU Berlin, and UMIST. The project is funded by the European Community represented by the CEC, Research Directorate-General, in the 6th Framework Programme, under Contract No. AST3-CT-2003-502842.

REFERENCES

- Batten, P., U. Goldberg, and S. Chakravarthy (2004). Interfacing statistical turbulence closures with large-eddy simulation. *AIAA Journal* 42(3), 485–492.
- Billson, M. (2004). *Computational Techniques for Turbulence Generated Noise*. Ph. D. thesis, Dept. of Thermo and Fluid Dynamics, Chalmers University of Technology, Göteborg, Sweden.
- Billson, M., L.-E. Eriksson, and L. Davidson (2004). Modeling of synthetic anisotropic turbulence and its sound emission. The 10th AIAA/CEAS Aeroacoustics Conference, AIAA 2004-2857, Manchester, United Kingdom, 2004.
- Buice, C. and J. Eaton (1997). Experimental investigation of flow through an asymmetric plane diffuser. Report No. TSD-107, Thermosciences Division, Department of Mechanical Engineering, Stanford University, Stanford, California 94305.
- Byun, G., R. Simpson, and C. H. Long (2004). A study of vortical separation from three-dimensional symmetric bumps. *AIAA Journal* 42(4), 754–765.
- Davidson, L. (2007). Using isotropic synthetic fluctuations as inlet boundary conditions for unsteady simulations. *Advances and Applications in Fluid Mechanics* 1(1), 1–35.
- Davidson, L. and M. Billson (2006). Hybrid LES/RANS using synthesized turbulence for forcing at the interface. *International Journal of Heat and Fluid Flow* 27(6), 1028–1042.
- Davidson, L. and S. Dahlström (2005a). Hybrid LES-RANS: An approach to make LES applicable at high Reynolds number. *International Journal of Computational Fluid Dynamics* 19(6), 415–427.
- Davidson, L. and S. Dahlström (2005b). Hybrid LES-RANS: Computation of the flow around a three-dimensional hill. In W. Rodi and M. Mulas (Eds.), *Engineering Turbulence Modelling and Measurements* 6, pp. 319–328. Elsevier.
- Davidson, L. and S.-H. Peng (2003). Hybrid LES-RANS: A one-equation SGS model combined with a $k-\omega$ model for predicting recirculating flows. *International Journal for Numerical Methods in Fluids* 43, 1003–1018.
- Emvin, P. (1997). *The Full Multigrid Method Applied to Turbulent Flow in Ventilated Enclosures Using Structured and Unstructured Grids*. Ph. D. thesis, Dept. of Thermo and Fluid Dynamics, Chalmers University of Technology, Göteborg.
- Jarrin, N., S. Benhamadouche, D. Laurence, and R. Prosser (2006). A synthetic-eddy-method for generating inflow conditions for large-eddy simulations. *International Journal of Heat and Fluid Flow* 27(4), 585–593.
- Klein, M., A. Sadiki, and J. Janicka (2003). A digital filter based generation of inflow data for spatially developing direct numerical or large eddy simulations. *Journal of Computational Physics* 186(2), 652–665.
- Kraichnan, R. (1970). Diffusion by a random velocity field. *Physics of Fluids* 13, 22–31.
- Le, H. and P. Moin (1994). Direct numerical simulation of turbulent flow over a backward facing step. Report no. TF-58, Stanford University, Dept. Mech. Eng.
- Lee, S., S. I. Lele, and P. Moin (1992). Simulation of spatially evolving turbulence and the application of Taylor's hypothesis in compressible flow. *Physics of Fluids* 4, 1521–1530.
- Pailhas, G., P. Barricau, Y. Touvet, and J. Monnier (2008). Turbulent separated flow through a channel with a bump (to be presented). In *EWA-UFAST workshop*, Prague.
- Smirnov, A., S. Shi, and I. Celik (2001). Random flow generation technique for large eddy simulations and particle-dynamics modeling. *Journal of Fluids Engineering* 123(2), 359–371.